Journal of Theoretical and Applied Information Technology
15th May 2025. Vol.103. No.9

ISSN: 1992-8645 www.jatit.org E-ISSN: 1817-3195

AUTOMATED SKIN LESION SEGMENTATION THROUGH HARMONIZING DERMOSCOPIC IMAGES WITH FUSION-BASED WHITE BALANCING

P. SHOBANA[1], J. DENY[2*], P. SWAPNA[3]

[1]Department of Electronics and Communication Engineering, Kalasalingam Academy of Research and Education, Virudhunagar, Tamil Nadu, India
[2*]Department of Electronics and Communication Engineering, Kalasalingam Academy of Research and Education, Virudhunagar, Tamil Nadu, India
[3]Department of Information Technology, Sethu Institute of Technology, Pulloor, Kariapatti, Virudhunagar District, Tamil Nadu, India
E-mail: [1]shobshobana@gmail.com, [2*]prof.j.deny@gmail.com, [3]swapnaengineer@gmail.com

ABSTRACT

To resolve aberrations resulting from the dominating single color channel in the RGB plane, this work presents a novel approach for dividing skin lesions in dermoscopic pictures. The accuracy of melanoma diagnosis is greatly impacted by these abnormalities; hence a thorough approach is required. The suggested method combines undesirable hair removal, white balance, and picture segmentation based on unsupervised learning. Two different picture versions are produced by using the Colour Equalisation approach and Shades of Grey Method after starting with the iterative Dull Razor approach for efficient depilation. Dermoscopic image analysis is enhanced by integration using a multi-scale image fusion approach, which promises better benign lesion classification and melanoma detection accuracy. By combining two color-corrected versions, creating conclusive skin lesion delineation by k-means clustering, and leveraging inherent textural information acquired through the Gabor filter, the multi-scale image fusion approach further improves the process. A very detailed picture of the skin lesion is produced by combining the resultant three-segmented images, demonstrating the complexity of this cutting-edge dermoscopic image processing technique.

Keywords: *Dermoscopic images, Skin lesion, Melanoma, Color correction, Image fusion, Color artifacts*

1. INTRODUCTION

To detect pigmented skin lesions, dermoscopy may be used as a non-invasive technique that uses magnification of skin images to examine the epidermis thoroughly. Nevertheless, dermoscopy does have a significant problem in that it might produce unwanted artifacts because pixel intensities vary unevenly between color channels. One successful technique for reducing artifacts caused by color dominance and picture noise is to use dermoscopy image preparation. Melanoma diagnosis relies heavily on this preprocessing phase for precise lesion segregation. When the tumor and healthy skin don't stand out in terms of color, making an accurate melanoma diagnosis becomes much more difficult. Because of this, preprocessing is crucial for improving diagnostic accuracy. Dermoscopy pictures still show skin hairs on lesions since manually removing them before imaging is not an option. Optimal augmentation of skin hairs is sometimes hindered by these photos, which often show them as dark or black. The refinement and enhancement of dermoscopic pictures therefore requires careful consideration of the existence of skin hairs.

The article lays out a new, simplified approach that starts with repeatedly waxing the affected area using the Dull Razors method. The next step is to deal with color dominance by combining versions of the same skin lesion picture that have been white-balanced. Dermoscopy pictures that are white-balanced are the product of skillful use of multiscale and multi-image fusion methods.

This article presents a new and simplified approach, starting with the repeated removal of skin hairs using a technique similar to the Dull Razors method. After that, the technique takes two white-balanced photos of the same skin lesion and merges them to fix the image's color dominance. By skilfully combining them, these two improved, white-

balanced dermoscopy images showcase the advantages of modern multiscale and multi-image fusion methods. To further fine-tune the disparity in pixel intensities across color channels, a locally calculated contrast weight is used.

The current research void, the manuscript unfolds as follows: Section 2 delves into an in-depth exploration of relevant studies, Section 3 outlines the envisioned methodology, Section 4 showcases experimental outcomes intertwined with comparative scrutiny, and Section 5 encapsulates the study's concluding remarks.

1.1. Contribution

- The extraction of hair is accomplished through the implementation of the Dull Razor technique.
- Utilizing the Color Equalization (CE) approach and the Shades of Grey (SOG) method, we extract modified inputs from a singular dermoscopy image.
- The derived iterations are amalgamated through the process of multiscale fusion, as outlined, yielding a version with a white balance.
- Skin lesion segmentation, involving the utilization of texture information, is carried out using the unsupervised k-means algorithm, in conjunction with the Gabor filter.

The three distinct segmented renditions of skin lesions within the same dermoscopic image are subsequently averaged to yield the ultimate segmented image.

2. RELATED WORKS

The utilization of image processing methods to scrutinize pertinent dermoscopy images facilitates the diagnosis of various skin diseases, irrespective of their benign or malignant nature and specific characteristics. This procedural step serves to diminish noise and rectify undesirable color distributions, thereby enhancing color contrast. Following the preprocessing phase, precise delineation of skin lesions occurs, leading to a clear identification of the underlying skin disease within the segmented region [1].

The concept of color correction finds application in various methods, including the traditional Gray World method [2], the Shades of Gray (SOG) method [3], techniques rooted in the Retinex theory [4], equalization of weak color channels to the predominant one in a method often referred to as Color Equalization (CE), and the assumption that in an ideal medium, the average color of a captured image should manifest as neutral gray within the RGB color plane.

In addressing the RGB image's color channels, the Lab color space and the HSV model channels were incorporated [5]. Color normalization of dermoscopic images was achieved by leveraging the dominant color channel, following Max-RGB and Grey-World principles from [6], as well as by reducing the mean pixel intensity of the image's color channel from [7]. The enhancement of dermoscopy images was performed using the multiscale top-hat transformation.

Jamil et al.'s methodology [8] for the segmentation of skin lesions, rooted in the dominant color space, particularly within the blue spectrum, was introduced. The standardization of color in dermoscopic images was meticulously executed through the Shades of Grey approach [9, 10]. Addressing illuminant fluctuations within dermoscopic images involved a sophisticated three-stage model [11]. Various techniques were harnessed for the enhancement of dermoscopic images, encompassing Histogram Equalization (HE), Burkhardt enhancement [12], Spatio-Temporal Retinex-inspired Envelope with Stochastic Sampling (STRESS) as evaluated by C. Olga et al. [13], Roy's enhancement [14], and the implementation of white balance [15]. Lesion segmentation was performed in [19], where the creation of an illumination-stable grayscale intrinsic image was achieved in [16] through entropy minimization. The delineation between the lesion and the surrounding skin was accentuated through the utilization of a sigmoidal function [17].

The features of a gradient applied to a specific type of image Gaussian distributed patterns-based image segmentation were performed in [18] where the obtained segmentation was not achieved compared to ground truth in some cases. In the realm of skin lesion segmentation, [19] employed gradient magnitude and morphological operations, although a notable limitation was the absence of a comparative analysis with the ground truth. Leveraging Transfer Learning and Fine-Tuning methodologies, [20] utilized U-Net and LinkNet for skin lesion segmentation. The U-Otsu method [21] found application in segmenting skin lesions within the YUV color space [22]. Furthermore, a distinctive approach involved skin lesion segmentation through the implementation of a multi-atlas method, with

subsequent accuracy enhancement achieved via the Bayesian framework [23].

In reference [24], a pioneering deep neural network, configured in a Siamese architecture and integrated with tensorial regression, was introduced to facilitate the short-term identification of melanoma lesions. This model strategically emphasizes global features over local details. In the realm of early melanoma diagnosis, [25] advocates for the utilization of a spatio-temporal network that leverages lesion progression information across consecutive dermoscopy images. Proposing an innovative approach, [26] suggests employing a bag-of-features model for melanoma identification, incorporating a learning strategy that combines a codebook with a histogram-based feature similarity measure.

In the ongoing pursuit of advancing melanoma identification methodologies, the work presented in [27] delves into a comprehensive exploration of the field. This study systematically investigates various architectural variants of Convolutional Neural Networks (CNN) along with the deployment of multiple classifiers. The overarching objective is to augment the precision and efficacy of melanoma detection. The nuanced approach taken reinforces the trajectory of innovation within this domain. Here, a distinctive deep network paradigm, structured in a Siamese configuration and augmented by tensorial regression, is revisited. Notably, this model is intricately designed with a specific emphasis on capturing global features, thereby enhancing its capability to discern short-term changes indicative of melanoma progression. The confluence of these advancements underscores the dynamic evolution of techniques aimed at improving the accuracy and reliability of melanoma identification within the realm of medical imaging and diagnostic research.

In the pursuit of refining melanoma classification, support vector machines (SVMs) were trained using the deep network features extracted from each image. The final prediction was achieved by aggregating the average prediction vectors from different Convolutional Neural Networks (CNNs). A distinctive approach is presented in [28], where the Morlet scattering transform is employed alongside CNNs for melanoma classification. This approach incorporates the assessment of skin roughness, determined from light field images, as a crucial third dimension in the classification process.

Aligned with the revelations expounded in [29], a transformative paradigm was posited in the domain of skin lesion recognition, harnessing the prowess inherent in a Convolutional Neural Network (CNN). This cutting-edge approach is aimed at automating the differentiation of diverse skin lesions based on their semantic features. To enhance the precision and efficacy of melanoma classification, a meticulous fine-tuning and optimization process was conducted on the Google Xception model, involving strategic additions of new layers, as elucidated in [30].

Moreover, the landscape of melanoma classification witnessed the introduction of sophisticated deep CNN models, employing an ensemble learning approach, as elucidated in [31] and [32]. These pioneering models were intricately designed to elevate the precision and reliability of melanoma diagnosis. Of notable mention is the successful classification achieved through the implementation of the SkinNet-16 model, rooted in a comprehensive set of ten distinct geometric and textural criteria, detailed in [33].

Simultaneously, the research focus on the intricate task of segmenting skin lesions in dermoscopic images has expanded. Deep learning-based techniques, exemplified by the application of UNet and its various adaptations, as outlined in [34-39], have emerged as promising methodologies. These techniques have opened innovative avenues for meticulous delineation and isolation of skin lesions in dermatoscopic images, thereby significantly enhancing diagnostic capabilities in the field of dermatology.

Upon scrutinizing the aforementioned studies and visualizing the insights presented in Figure 1, it becomes evident that the diagnostic performance of image processing-based methods is substantially influenced by the presence of color artifacts and hairs in dermoscopic images. Particularly challenging are skin lesions exhibiting color intensities closely mirroring normal skin, thereby posing a formidable obstacle in distinguishing these lesions from healthy skin when employing dermoscopy for diagnostic purposes.

The collective findings from the various studies we've discussed, along with the insights provided in Figure 1, the substantial impact of color artifacts and the presence of hair in dermoscopic images on the efficacy of image processing-based diagnostic methods. These factors play a pivotal role in determining how accurately such methods can differentiate between malignant skin lesions and healthy skin.

In particular, the challenge arises when skin lesions exhibit a color intensity that closely mimics that of normal skin. In such cases, the boundary

Journal of Theoretical and Applied Information Technology
15th May 2025. Vol.103. No.9

ISSN: 1992-8645 www.jatit.org E-ISSN: 1817-3195

between pathological lesions and healthy skin becomes increasingly ambiguous, making it more difficult for dermoscopy-assisted diagnostic systems to provide accurate results.

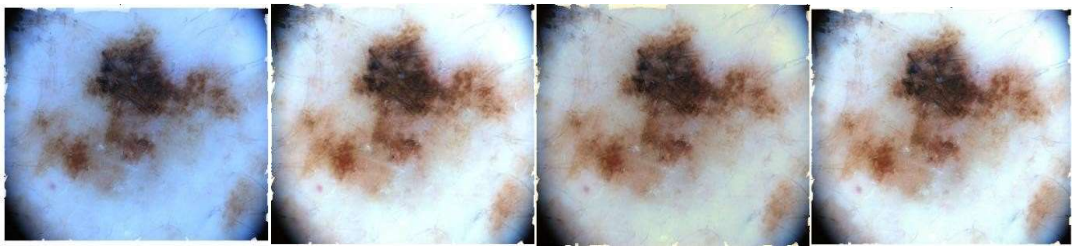

(a)

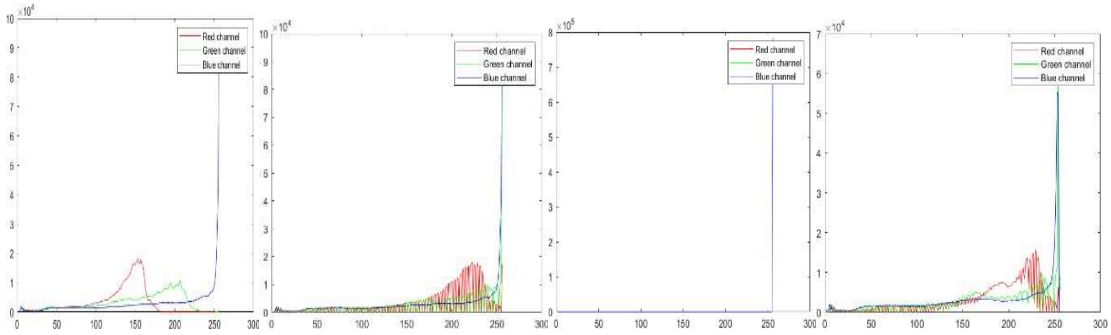

(b)

Figure 1: Histogram of Dermoscopic image

To delve deeper, the color artifacts inherent in dermoscopic images can introduce incongruities in color, saturation, and contrast, thereby posing challenges for automated diagnostic algorithms. Simultaneously, the presence of hairs on the skin's surface introduces shadows and textural variations, further complicating the analytical process. These intricacies collectively underscore the imperative need for advanced image processing techniques capable of mitigating the adverse effects of color artifacts and hairs in dermoscopic images, consequently elevating the precision of skin lesion diagnosis.

3. PROPOSED METHOD

This groundbreaking research presents a cutting-edge two-phase methodology, specifically designed to tackle the persistent challenge of red color imbalance in dermoscopic images a bottleneck frequently identified in earlier methodologies dedicated to image enhancement, such as those referenced in literature. The overarching objective of this innovative approach is to overcome the limitations observed in prior methods, which struggled to achieve precise skin lesion segmentation due to the complexity introduced by red color imbalance. In the initial phase, the methodology focuses on rectifying the red color imbalance, a critical issue that has often impeded accurate segmentation in previous studies.

This involves the development of advanced techniques tailored to address the unique characteristics of dermoscopic images, paving the way for more effective image enhancement. The second phase strategically builds upon the corrections made in the first, directing attention toward achieving precise skin lesion segmentation. Leveraging insights gained from the rectification of color imbalance, this phase employs sophisticated algorithms and strategic methodologies to enhance the accuracy of lesion segmentation. By systematically addressing both color imbalance and segmentation challenges, this two-phase approach aims to establish a robust foundation for more effective and reliable skin lesion identification in dermoscopic images, marking a significant advancement in the field.

To elucidate this methodology, a visual representation in the form of a flowchart is employed to elucidate the intricate processes of rectifying white balance and executing image segmentation, as depicted in Figure 2. Commencing with a dual-pronged strategy, the primary objective is to rectify the white balance intricacies inherent in Dermoscopic images. Two discrete color constancy

techniques are meticulously applied independently to the same set of Dermoscopic images, yielding two distinct iterations with impeccably balanced color tones. Subsequently, a fusion process ensues, leveraging the weighted multi-scale image fusion technique. This technique adeptly amalgamates the two color-corrected images, resulting in a third iteration that achieves a heightened level of refined white balance.

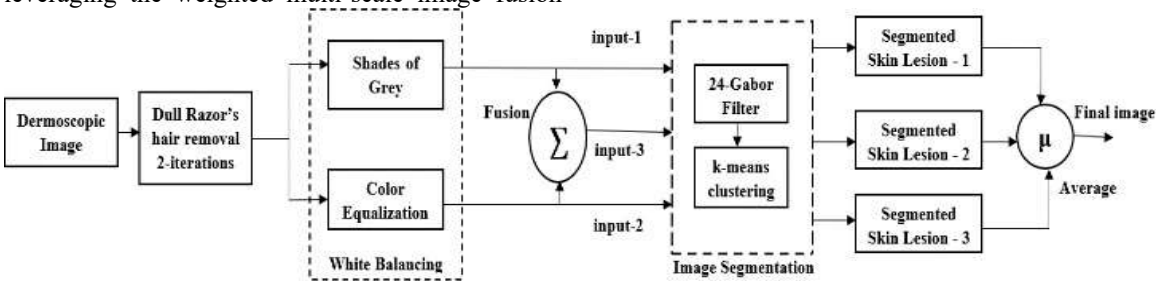

Figure 2: Flow chart of the proposed method

Moving to the subsequent stage, the emphasis transitions to the nuanced undertaking of segmenting skin lesions. This entails the skillful application of image segmentation methodologies rooted in texture features. To distinguish the lesion area from the trio of color-corrected dermoscopic images, intricate texture information is extracted with precision utilizing the Gabor filter. Subsequently, the k-means clustering algorithm is employed to perform the necessary segmentation. The culmination involves averaging the results from the three-segmented images in their binary form, producing a meticulously delineated region corresponding to the skin lesion.

3.1. White Balancing

Delving deeper into the realm of white balancing, we expound upon the rationale behind the application of color equalization and shades of grey, intricately discussed in the preceding section. Color equalization serves as a pivotal technique, rectifying variations in color intensity within an image by leveraging comprehensive information on the mean intensity in each color space. This process harmonizes and equalizes the distribution of color, optimizing visual coherence.

Contrastingly, the concept underlying shades of grey transcends a mere greyscale transformation. It entails the calculation of the mean intensity for a normalized image, resulting in a unique shade of grey that encapsulates the nuanced essence of the image's color balance. When strategically combined, the synergy between color equalization and shades of grey yields a potent approach. This fusion markedly enhances the quality and precision of each dermoscopic image, notably augmenting their appropriateness for the crucial undertaking of skin lesion segmentation.

3.2. Color Equalization

Dermoscopic images frequently exhibit a pronounced prevalence of the red color component. This equalization process involves careful adjustments to the less dominant color channels to harmonize them with the prevailing one, usually the red channel. It is essential to note that the dominance of color in dermoscopic images may exhibit variations depending on the specific lighting conditions employed during imaging. In more detail, meticulous adjustments are applied to the color channels that are less prominent in the dermoscopic images. The goal is to create a balanced and coherent representation where all color channels align harmoniously with the prevailing red channel. This harmonization process is crucial for ensuring uniformity and consistency in color representation, which is particularly sensitive in dermoscopic images. Importantly, variations in the dominance of color can be attributed to the diverse lighting conditions used during the imaging process, further emphasizing the need for adaptive equalization techniques to accommodate these variations and maintain the accuracy of subsequent analyses or processing steps.

In instances where the dominance shifts toward the blue spectrum due to specific lighting characteristics, a judicious color equalization procedure is set into motion. This procedure meticulously aligns the red and green color channels with the blue channel, ensuring a more uniform and balanced color representation.

i) Conversely, in scenarios where the average intensity of the red channel exceeds that of the blue and green channels, the equalization process is tailored to favor the red channel. This adaptive approach ensures a consistent optimization of color balance, resiliently accommodating fluctuations in color dominance across diverse dermoscopic images.

$$J_{gc}(y,z) = \left(\frac{J_r^m(y,z)}{J_g^m(y,z)}\right) \times J^G(y,z) \quad (1)$$

$$J_{bc}(y,z) = \left(\frac{J_r^m(y,z)}{J_b^m(y,z)}\right) \times J^B(y,z) \quad (2)$$

ii) if the average intensity of blue color light is higher, then red and green channels are equalized by,

$$J_{rc}(y,z) = \left(\frac{J_b^m(y,z)}{J_r^m(y,z)}\right) \times J^R(y,z) \quad (3)$$

$$J_{gc}(y,z) = \left(\frac{J_b^m(y,z)}{J_g^m(y,z)}\right) \times J^G(y,z) \quad (4)$$

Here $J_{rc}(y,z)$, $J_{gc}(y,z)$ $J_{bc}(y,z)$ are color manipulated versions of red, green, and blue respectively. Correspondingly $J_r^m(y,z)$, $J_g^m(y,z)$ and $J_b^m(y,z)$ denote the average pixel intensities of their respective color spaces within $J(y,z)$.

3.3. Shades of Grey

The average scene is believed to have a somewhat different shade of grey from absolute grey. This presumption might be formed by

$$\mu_p(S(\lambda)) = \left[\sum_{j=1}^{M} \frac{\{S_i(\lambda)\}^p}{M}\right]^{1/p} = k_p \quad (5)$$

In this, μ is the average scene radiance, $S(\lambda)$ signifies the Lambertian surface, M represents image dimension, k is the illuminant color constant, and here p represents the Minkowski norm. (3) is extended to the three-color channels and they are individual equations:

$$\mu_p(r_p) = \left[\int E_p(\lambda)\left(\sum_{j=1}^{M} \frac{\{S_i(\lambda)\}^p}{M}\right) r(\lambda)d\lambda\right]^{1/p} = k_p r_e \quad (6)$$

$$\mu_p(g_p) = \left[\int E_p(\lambda)\left(\sum_{j=1}^{M} \frac{\{S_i(\lambda)\}^p}{M}\right) g(\lambda)d\lambda\right]^{1/p} = k_p g_e \quad (7)$$

$$\mu_p(b_p) = \left[\int E_p(\lambda)\left(\sum_{j=1}^{M} \frac{\{S_i(\lambda)\}^p}{M}\right) b(\lambda)d\lambda\right]^{1/p} = k_p b_e \quad (8)$$

This $E(\lambda)$ shows the spectral distribution, while $r(\lambda)$, $g(\lambda)$ and $b(\lambda)$ denotes the signals of red, green, and blue additionally r_e, g_e and b_e represents the constancy of respectively red, green, and blue channels. (3) can reduce to the Grey-World method, if $p = 1$. And (3) follows the max-RGB method, if $p = \infty$ and hence Minkowski norm is limited as $1 < p < \infty$. for shades of grey and a better result, the value is, $p = 5$.

3.4. Multiscale Image Fusion

The luminance (L-channel) undergoes Laplacian filtering, to enhance edge details and fine-tune contrast. To emphasize the distinctions between areas with gradual transitions and flat regions, the global contrast weight G_{wg}^j is incorporated into the Laplacian contrast weight map. The computation of the local contrast weight L_{wg}^j is expressed as:

$$L_{wg}^j = \left\| i_l^j - i_{lp}^j \right\| \quad (9)$$

Here i_l^j and i_{lp}^j represent the luminance of the jth input, in this example $j = 1\ and\ 2$, along with their low passed versions, respectively. By passing them i_{lp}^j through a filter, they i_l^j can be obtained [0.0625, 0.25, 0.375, 0.25, 0.0625] binomial kernel binomial. The frequency falls within the specified cut-off range, $l_p = 1.14182$. The resultant image undergoes a blurring process facilitated by a three-Gaussian filter. Subsequently, the output is transposed to the Lab color domain, where the weight of the saliency map S_{wg}^j is calculated.

$$S_{wg}^j = (L - L_m)^2 + (a - a_m)^2 + (b - b_m)^2 \quad (10)$$

Where the three planes' images in the $L * a * b *$ domain are $L, a, and\ b$. The average values of the $L, a, and\ b$ planes are L_m, a_m and b_m. The enhancement of the fused image quality can be achieved by applying a weight to the exposedness map E_{wg}^j, which is provided by,

Journal of Theoretical and Applied Information Technology
15th May 2025. Vol.103. No.9

ISSN: 1992-8645 www.jatit.org E-ISSN: 1817-3195

$$E_{wg}^{j} = \exp\left(\frac{(-(I^{j}(y,z) - 0.5)^2)}{2 \cdot \sigma^2}\right) \quad (11)$$

Here $I^{j}(y,z)$ is the pixel intensity of jth input image at (y,z) coordinates. Here we let $\sigma = 0.25$. The weight of the normalized map n_{wt}^{j} is used to get consistent results under the hypothesis that the total of all weight maps at every one of the pixel coordinates equals 1.

$$n_{wt}^{1} = \frac{G_{wg}^{1} + L_{wg}^{1} + S_{wg}^{1} + E_{wg}^{1}}{G_{wg}^{1} + L_{wg}^{1} + S_{wg}^{1} + E_{wg}^{1} + G_{wg}^{2} + L_{wg}^{2} + S_{wg}^{2} + E_{wg}^{2}} \quad (12)$$

$$n_{wt}^{2} = \frac{G_{wg}^{2} + L_{wg}^{2} + S_{wg}^{2} + E_{wg}^{2}}{G_{wg}^{1} + L_{wg}^{1} + S_{wg}^{1} + E_{wg}^{1} + G_{wg}^{2} + L_{wg}^{2} + S_{wg}^{2} + E_{wg}^{2}} \quad (13)$$

The original and normalized weight maps are shown in Fig.3 and 3a.

Figure 3: Original image

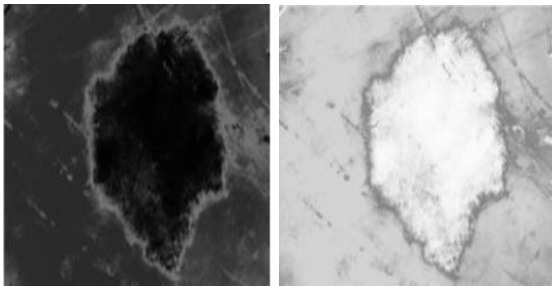

Figure 3 (a): Images of normalized weight maps

The two-color corrected image is next convolved through a kernel of five-level Gaussian, a laplacian, and an operator [0.0625, 0.25, 0.375, 0.25, 0.0625] to generate low-pass and band-passed versions, respectively. At last, a higher resolution variant of the image J(y,z) is generated by,

$$J(y,z) = \sum_{j=1}^{2} \sum_{k=1}^{5} g^{k}\{n_{wt}^{j}\} \times l^{k}\{i^{C}(y,z)\} \quad (14)$$

Here k denotes the number of pyramid levels, j denotes the number of derived input images, $g\{n\}$ symbolizes the Gaussian pyramid of the normalized weight map, and $\{i\}$ signifies the Laplacian pyramid.

3.5. 2-Dimensional Gabor Filter

The Gabor filter, initially introduced by Gabor, is a method for characterizing image textures by analyzing them in the frequency domain. It operates by modulating a complex sinusoidal waveform concerning frequency and orientation using a Gaussian function. This modulation occurs in both the frequency and time domains. The Gabor filter, being suitable for textures with slight variations, analyzes an image by Fourier transforming it and then convolving it with a Gaussian function having different frequency centers. The resulting output is then subjected to an inverse fast Fourier transform (IFFT). The 2-D Gabor filter is constructed with a Gaussian function modulated by a complex sinusoidal waveform of frequency and orientation [26]. Its representation is articulated as:

$$G(y,z) = e^{-\frac{(y-y_0)^2}{2\sigma_y^2} - \frac{(z-z_0)^2}{2\sigma_z^2}} e^{j(\omega_{y0}y + \omega_{z0}z)} \quad (15)$$

The coordinates of pixels are denoted by (y, z), where σ_y and σ_z express the standard deviation of the Gaussian function beside the y and z directions, respectively. Here the center frequencies for the y and z directions, denoted as ω_{y0} and ω_{z0}, correspond to the locations with the highest responses to the filter. With a total of l = 6 orientations, the bandwidth of orientation ($\Delta\theta$) is calculated, $\Delta\theta = \frac{360}{8} = 45° = 0.7854\,rad$. Thus, the orientation, θ are 0°,45° and 135°. The centre of frequency C is given by:

$$\rho_C = \frac{\omega_C + \omega_{C-1}}{2} = \frac{1}{2}(2^{C}\omega_0 - 2^{C-1}\omega_0) = 2^{C-1} \cdot 3\omega_0 \quad (16)$$

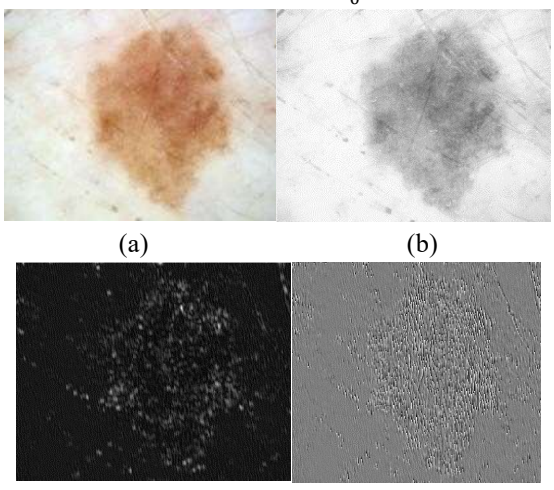

(a) (b) (c) (d)

Figure 4: Magnitude and Phase of Gabor filter for wavelength 4 and Orientation 90°. (a) Original image (b) Greyscale of original (c) Gabor magnitude (d) Gabor phase

In the realm of image analysis, a set of 24 Gabor filters, each characterized by four distinct orientations, is applied to process an input image measuring 516 by 516 in dimensions. Figure 4 (a), (b), (c), and (d) provide a visual representation of the amplitude, phase, and orientation of the Gabor filter, specifically for the wavelength.

3.6. k-means clustering

Transitioning to the concept of clustering, clustering refers to the process of partitioning a dataset into a predetermined number of smaller groups. A widely employed clustering method is the k-means clustering approach, which involves dividing the dataset into k clusters. The k-means clustering process unfolds in two key stages. It begins by calculating the centroid for each cluster, followed by the assignment of data points to the cluster whose centroid is nearest to them. Typically determined using Euclidean distance. After the clustering has been established, there is a recalculation of the Euclidean distance between each centroid and data point. Subsequently, the data point is assigned to the cluster with the smallest distance.

Every cluster is characterized by its distinct set of data points, with a centroid representing its central position. The fundamental goal of k-means clustering is to minimize the collective distance between all data points within a cluster and the corresponding cluster centroid, which effectively serves as an additional data point. The iterative nature of k-means clustering is focused on achieving this minimization of distances throughout the process.

Considering this image $J(y,z)$ to be subjected to clustering into two clusters (k=2) to partition the Dermoscopic image into two segments: one comprising the skin lesion and the other containing normal skin. Let $p(y,z)$ represent the input pixels to be clustered, and c^k denote the center of the clusters. The procedural steps in k-means clustering are delineated in Figure. 4 and also enumerated as follows:

1. Initialization involves selecting the required number of clusters, k, and defining the initial centroids.

2. The calculation of the Euclidean distance, denoted as 'd,' between each pixel and the center is determined by the formula:

$$D = \|p(y,z) - c^k\| \quad (17)$$

3. Based on the calculated distances (D), assign each pixel to the nearest centroid.

4. Subsequently, update the centroid's position using the formula:

$$c^k = \frac{1}{k} \sum_{z \in c^k} \sum_{y \in c^k} p(y,z) \quad (18)$$

5. Iteratively repeat the process until the sum of variances reaches its minimum.

6. Finally, reshape the clustered pixels to reconstruct the image.

4. RESULTS AND DISCUSSION

The implementation of this proposed methodology was carried out using MATLAB R2020a, leveraging an Intel i3 processor with 8GB of RAM. The assessment utilized a demanding image dataset obtained from the releases of the International Skin Imaging Collaboration (ISIC). The dataset encompassed a total of 900, 2000, and 2594 images extracted from the releases in 2016, 2017, and 2018, respectively.

4.1 Qualitative Assessment

The outcomes of the implemented method are visually presented in Figure 5. In Figure 5(a), the original skin lesion images, characterized by lower quality, are illustrated. Following this, Figures (b), (c), (d), and (e) depict the images after undergoing various enhancements. These enhancements include hair removal using Dull Razor's method, color equalization, grayscale transformation, and the combination of color equalization (CE) with shades of gray (SOG).

Particularly, the enhancement achieved through the blending of CE and SOG produces well-balanced images without any artifacts. In the original images displayed in Figure 5(a), you can observe the presence of red and blue color dominance. However, the proposed method effectively eliminates this dominance, as depicted in Figure 5(e). As a result, this approach surpasses the previous methods by offering improved color contrast and clear differentiation between the lesions and normal skin.

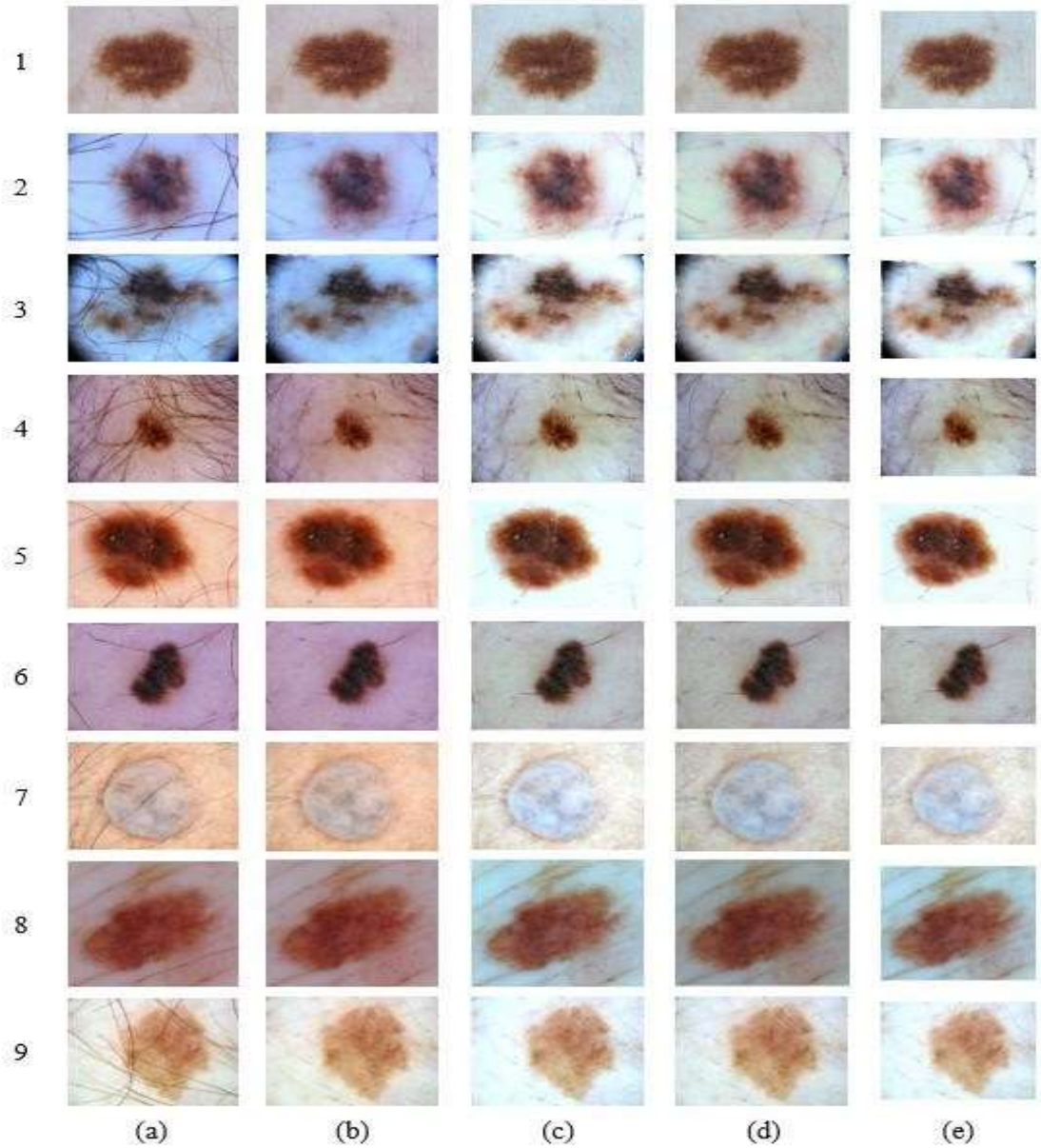

Figure 5: Comparison of existing methods for enhancement of melanoma images (a) original image, (b) Dull Razor's result (c) result of Color Equalization (d) result of Shades of Grey, and (e) blending of (c) and (d)

4.2 Quantitative Assessment

The segmentation approach proposed for distinguishing skin lesions in dermatoscopic images is elucidated in Figure 6. Figure 6(a) provides an overview of the original dermoscopic images. Moving forward, Figure 6(b) showcases the binary ground truth version, while Figures 6(c), (d), (e), and (f) Respectively, Figures 6(c), (d), (e), and (f) depict the binary images resulting from color equalization (CE), shades of gray (SOG), the fused version of both, and the average image from all three versions. To gauge the efficacy of the proposed method and validate it against existing approaches, various metrics are employed. These include the Jaccard Index (JI), Dice Coefficient (DI) (known to be F1-Score), Precision, Recall, and Boundary F1-Score (BF Score). The Jaccard Index (JI) quantifies the ratio of the overlapping area to the union of two similar images. It serves as a metric to assess the concordance between the ground truth and the resulting image.

$$JI = \frac{\text{Area of Overlap}}{\text{Area of Union}} \quad (19)$$

The Jaccard Index (JI) is bounded within the range of 0 to 1, where JI = 0 signifies no overlapping, and JI = 1 indicates full overlapping.

The F1-Score, encompassing the same range of 0 to 1, can be characterized as follows: 0≤F1-Score≤1.

$$F1-\text{Score} = 2 \times \frac{\text{Area of Overlap}}{\text{Total no. of pixels in both images}} \quad (20)$$

It indicates the similarity i.e., the F1-Score =1 implies that the two images are mostly similar. The closeness of matching of boundaries of two images can be predicted using the BF Score.

$$\text{BF Score} = 2 \times \frac{\text{Precision} \times \text{Recall}}{\text{Precision} + \text{Recall}} \quad (21)$$

The precision provides the rate of true positive detection concerning total positive and is given by,

$$\text{Precision} = \frac{\text{true positive}}{\text{true positive} + \text{false positive}} \quad (22)$$

The recall gives the true positive detection concerning true positive and false negative and is given by:

$$\text{Recall} = \frac{\text{true positive}}{\text{true positive} + \text{false negative}} \quad (23)$$

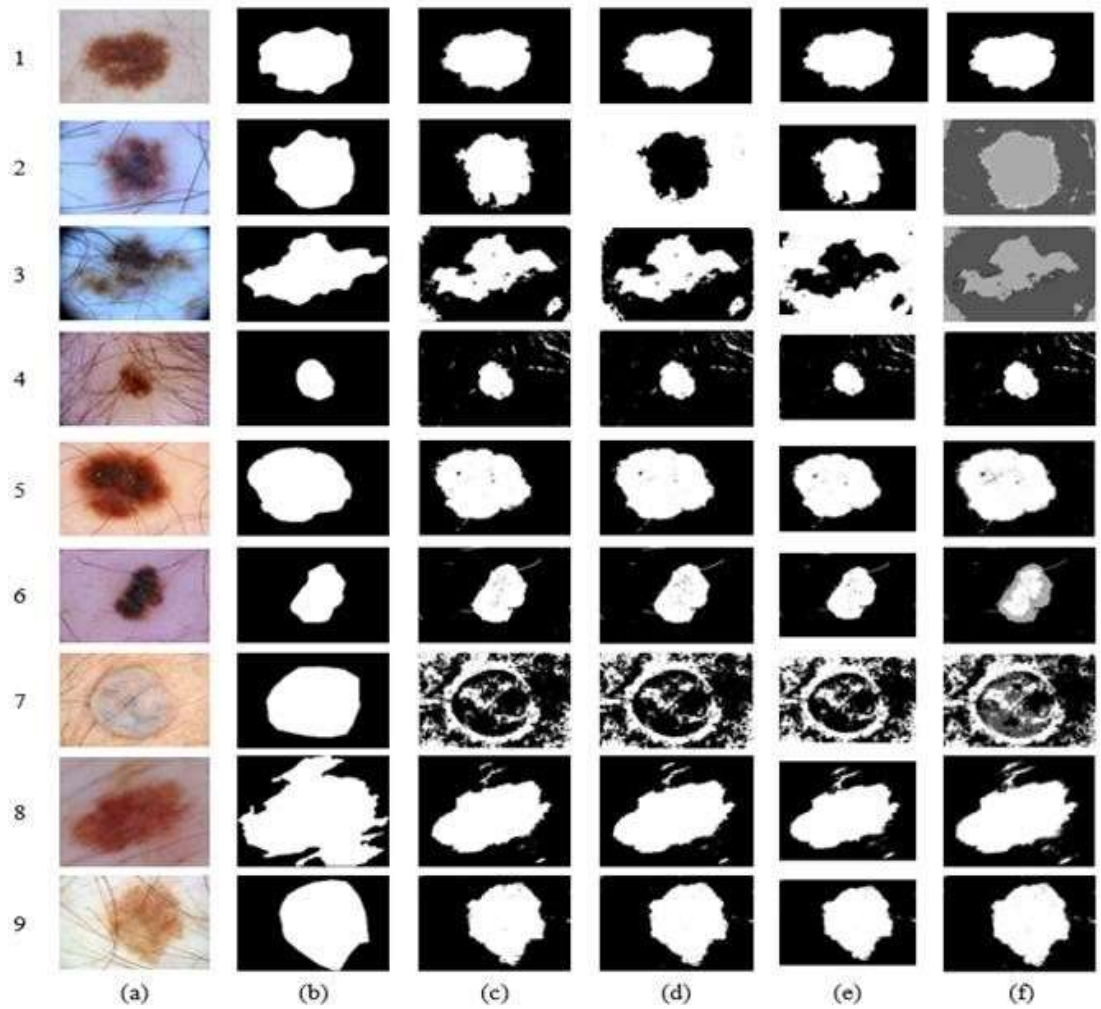

Figure 6: Comparison Studies of Segmentation (a) original image, (b) Ground truth image, (c) CE version and (d) SOG version, and (e) blending of (c) and (d) and f) average of (c), (d) and (e)

Both precision and recall metrics have values within the range of 0 to 1, representing their effectiveness. In Table I, you can find the specific values for the Jaccard Index (JI), Dice Coefficient (DI), Precision, Recall, and Boundary F1-Score (BF Score). Upon analyzing Table I, it becomes evident that the average binary image created by the proposed method, utilizing shades of gray, color equalization, and their fused version, achieves a notably high score compared to the approach involving the blending of CE and SOG. However, it is crucial to acknowledge a limitation in the proposed method, specifically in accurately segmenting certain areas. Dominated by the color

blue, as indicated by the lower scores in terms of BF Score, Precision, and Recall.

4.3 Comparative Analysis

In this study, we undertook a performance comparison of our proposed method against several existing techniques, including UNet [61], CPF-Net [62], CE-Net [63], FAT-Net [64], and EI-UNet [65]. To validate and benchmark the performance, we employed the Jaccard Index and Dice Index. The assessment encompassed datasets from ISIC 2016, ISIC 2017, and ISIC 2018.

4.3.1 Study with ISIC Dataset 2016

The results for both the proposed method and the aforementioned existing techniques (UNet, CPF-Net, CE-Net, and EI-UNet) are presented in Figure 7. In this figure, the red line represents manual skin lesion markings, while the black line indicates the segmentation produced by the various methods.

The quantitative experimental results are concisely summarized in Tables I and II. Our proposed method achieves a Jaccard Index of 0.847 and a Dice Score of 0.901 for the ISIC 2016 dataset. In comparison, UNet, CPF-Net, CE-Net, FAT-Net, and EI-UNet exhibit average Jaccard Index scores of 0.836, 0.842, 0.846, 0.853, and 0.855, respectively. It is noteworthy that for the ISIC 2016 dataset, EI-UNet outperforms UNet, CPF-Net, and CE-Net in terms of the Jaccard Index. For the Dice Score, EI-UNet stands out with a score of 0.919, while our proposed method achieves a score of 0.901. Conversely, UNet, CPF-Net, CE-Net, and FAT-Net achieve Dice Scores of 0.903, 0.907, 0.909, and 0.916, respectively.

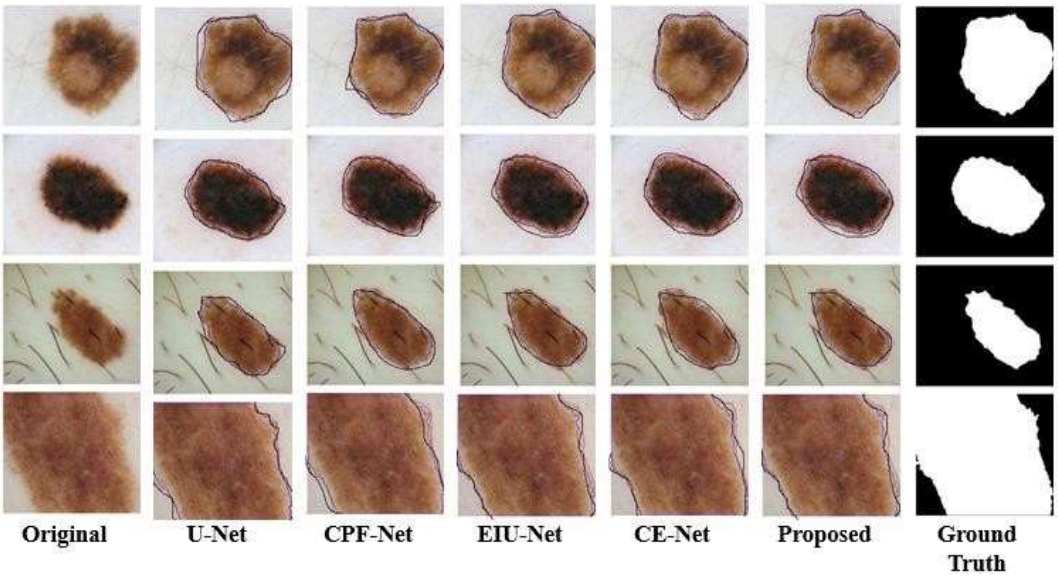

Figure 7: Experimental Results with ISIC 2016 Dataset

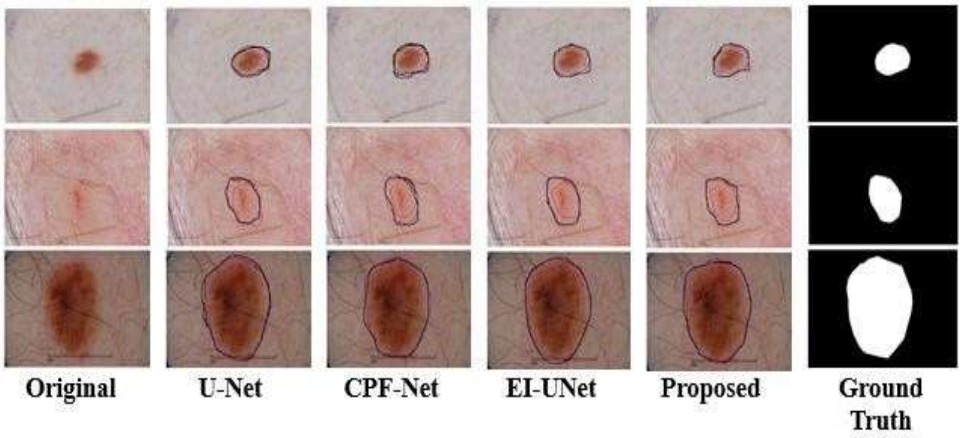

Figure 8: Experimental Results with ISIC 2017 Dataset

4.3.2 Study with ISIC Dataset 2017

We conducted a comparative analysis with ISIC Dataset 2017, pitting our proposed method against CE-Net, FAT-Net, and EI-UNet. The Dice-Scores achieved were 0.828, 0.847, 0.848, 0.850, and 0.855 for CE-Net, FAT-Net, EI-UNet, UNet, CPF-Net, and our method, respectively. Notably, EI-UNet excelled in the Jaccard Index with a score of 0.771, outperforming the others. In contrast, UNet, CPF-Net, CE-Net, FAT-Net, and our proposed method scored 0.737, 0.762, 0.764, 0.765, and 0.689 in the shown in Figure 8 Jaccard Index, respectively.

It's essential to highlight that our proposed method showed a lower Jaccard Index for ISIC Dataset 2017 compared to other methods discussed in this article. However, it demonstrated strong performance in terms of the Dice Score.

CE-Net, FAT-Net, and EI-UNet achieve the Dice-Score as 0.828, 0.847, 0.848, 0.850, and 0.855 respectively. The EI-UNet achieves 0.771 Jaccard Index and outperforms well whereas the methods UNet, CPF-Net, CE-Net, FAT-Net, and the proposed method achieve the Jaccard Index of 0.737, 0.762, 0.764, 0.765 and 0.689 respectively. The proposed method achieves a poor Jaccard Index for ISIC Dataset 2017 compared to other methods discussed in this article whereas in terms of Dice-Score, the proposed method reaches good performance.

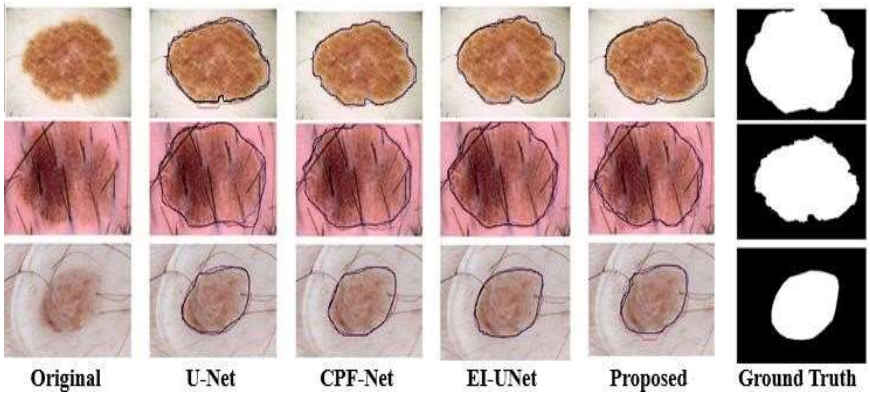

Figure 9: Experimental Results with ISIC 2018 Dataset

Table 1: Quantitative Analysis with Color Constancy Algorithms.

No.	Performance Metrics									
	JI		DI		BF Score		Precision		Recall	
	Resultant Image Types									
	Average	Fusion	Average	Fusion	Average	Fusion	Average	Fusion	Average	Fusion
1	0.8541	0.8522	0.9214	0.9202	0.1675	0.1626	0.1242	0.1191	0.2582	0.2564
2	0.3345	0.8102	0.5013	0.8952	0.1523	0.2933	0.1345	0.2322	0.8546	0.3979
3	0.3626	0.0929	0.5323	0.1700	0.1819	0.1612	0.1168	0.0998	0.4116	0.4192
4	0.7041	0.6812	0.8263	0.8104	0.2421	0.1525	0.1413	0.0882	0.8475	0.5608
5	0.9389	0.8742	0.9685	0.9329	0.6581	0.1784	0.5120	0.1106	0.9209	0.4619
6	0.9057	0.8999	0.9505	0.9473	0.6190	0.5599	0.4556	0.3943	0.9651	0.9651
7	0.3892	0.1690	0.5604	0.2891	0.0440	0.0575	0.0230	0.0299	0.5037	0.7123
8	0.6269	0.5789	0.7707	0.7333	0.0265	0.0067	0.0204	0.0058	0.0381	0.0081
9	0.7488	0.7476	0.8564	0.8556	0.0207	0.0063	0.0128	0.0035	0.0538	0.0320

4.3.3 Study with ISIC Dataset 2018

Moving on to the assessment with the ISIC Dataset 2018, we conducted both qualitative and quantitative comparisons with existing methods, including UNet, CPF-Net, and EI-Net. Figure 9 presents the resulting images, with the red line indicating manual skin lesion markings and the black line representing the segmentations proposed by various methods.

Table 2: Comparative Evaluation of the Proposed Approach with Other Methods.

Method	JI			DI		
	IMAGE DATASET					
	ISIC 2016	ISIC 2017	ISIC 2018	ISIC 2016	ISIC 2017	ISIC 2018
UNet [61]	0.836	0.737	0.810	0.903	0.828	0.879
CPF-Net [62]	0.842	0.762	0.826	0.907	0.847	0.893
CE-Net [63]	0.846	0.764	0.825	0.909	0.848	0.893
FAT-Net [64]	0.853	0.765	0.833	0.916	0.850	0.899
EI-UNet [65]	**0.855**	**0.771**	0.836	**0.919**	0.855	**0.902**
Proposed	0.847	0.689	**0.854**	0.901	**0.862**	0.801

When quantitatively comparing our proposed method with UNet, CPF-Net, CE-Net, FAT-Net, and EI-UNet in terms of Dice-Score and Jaccard Index, In our observations, EI-UNet demonstrated superior performance with a Dice-Score of 0.902. UNet, CPF-Net, CE-Net, FAT-Net, and our proposed method achieved Dice-Scores of 0.879, 0.893, 0.893, 0.899, and 0.801, respectively. Our proposed method excelled in terms of the Jaccard Index, achieving a score of 0.854. For comparison, UNet, CPF-Net, CE-Net, FAT-Net, and EI-UNet obtained Jaccard Index scores of 0.810, 0.826, 0.825, 0.833, and 0.836, respectively. It's important to note that our proposed method exhibited a relatively lower Dice Score for ISIC Dataset 2018 compared to the other methods discussed in this article. However, in terms of the Jaccard Index, our proposed method demonstrated strong performance.

5. CONCLUSION

In conclusion, our proposed method, which integrates hair removal, color correction, and multi-scale image fusion-based white balancing, offers a comprehensive approach to enhancing dermoscopic images for accurate skin lesion segmentation. By applying Gabor filter-based k-means clustering to extract texture features, we were able to segment skin lesions across three enhanced versions of the same dermoscopic image. The final step of averaging the binary versions of these three segmented images contributed to highly accurate and consistent lesion segmentation. Our results demonstrate that this multi-faceted enhancement approach outperforms individual image enhancements, showcasing its strong potential in advancing dermatological image analysis.

Our findings provide significant insight into the importance of combining multiple image processing techniques to improve segmentation accuracy. The use of multi-scale image fusion for white balancing, alongside advanced texture extraction through Gabor filtering, appears to offer a robust solution for improving the quality of dermoscopic images and segmenting skin lesions more effectively than conventional methods.

However, there are several areas where future research could build upon this work. First, exploring the scalability of this method for a wider range of skin types, lesion types, and lighting conditions could help determine its robustness and applicability in diverse real-world clinical settings. Additionally, while the use of three enhanced images showed promising results, further investigating the optimal number of images or advanced fusion techniques could potentially increase segmentation accuracy. Incorporating more advanced machine learning or deep learning techniques for texture feature extraction and segmentation might also yield even better results, especially when working with large datasets. Lastly, testing this method on a larger, more diverse dataset would provide further validation and help in addressing any limitations related to the variability of dermoscopic images across different demographics and devices.

In summary, this work offers a promising approach to skin lesion segmentation and enhances the potential for automated dermatological diagnosis, though further research is needed to refine and extend these techniques for broader and more varied clinical applications.

REFERENCES:

[1] S. M. Pizer, R. E. Johnston, J. P. Ericksen, B. C. Yankaskas and K. E. Muller, "Contrast-limited adaptive histogram equalization: speed and effectiveness," *Proceedings of the First Conference on Visualization in Biomedical Computing, Atlanta, GA, USA*, 1990, pp. 337-345.

[2] M. Ebner, *Color constancy*. 2007. Available: https://www.amazon.com/Color-Constancy-Marc-Ebner/dp/0470058293

[3] G. D. Finlayson and E. Trezzi, "Shades of gray and colour constancy," *Color and Imaging Conference*, Vol. 12, No. 1, 2004, pp. 37–41.

[4] E. H. Land, "The Retinex Theory of Color Vision," *Scientific American*, Vol. 237, No. 6, 1977, pp. 108–128.

[5] Y. Yuan and Y.-C. Lo, "Improving dermoscopic image segmentation with enhanced Convolutional-Deconvolutional networks," *IEEE Journal of Biomedical and Health Informatics*, Vol. 23, No. 2, 2017, pp. 519–526.

[6] G. Schaefer, M. I. Rajab, M. E. Celebi and H. Iyatomi, "Skin lesion extraction in dermoscopic images based on colour enhancement and iterative segmentation," *2009 16th IEEE International Conference on Image Processing (ICIP), Cairo, Egypt, 2009*, pp. 3361-3364.

[7] J. C. Mello-Román et al., "Dermoscopy images enhancement via Multi-Scale morphological Operations," *Applied Sciences*, Vol. 11, No. 19, 2021, p. 9302.

[8] U. Jamil, S. Khalid and M. U. Akram, "Dermoscopic image enhancement and hair artifact removal using Gabor wavelet," *2016 Sixth International Conference on Innovative Computing Technology (INTECH), Dublin, Ireland*, 2016, pp. 279-284.

[9] M. Goyal, A. Oakley, P. Bansal, D. Dancey, and M. H. Yap, "Skin lesion segmentation in dermoscopic images with ensemble deep learning methods," *IEEE Access*, Vol. 8, 2019, pp. 4171–4181.

[10] P. Shobana and J. Deny, "U-Net Based Segmentation of Skin Lesions Using Dermoscopic Images," *2023 2nd International Conference on Vision Towards Emerging Trends in Communication and Networking Technologies (ViTECoN), Vellore, India*, 2023, pp. 1-5.

[11] J. Glaister, R. Amelard, A. Wong, and D. A. Clausi, "MSIM: Multistage Illumination Modeling of Dermatological Photographs for Illumination-Corrected Skin Lesion Analysis," *IEEE Transactions on Biomedical Engineering*, Vol. 60, No. 7, 2013, pp. 1873–1883.

[12] B. J, "IMAGE CONTRAST. Enhance contrast of an image," 2010. [Online]. Available: https://people.sc.fsu.edu/_jburkardt/msrc/image contrast/image contrast.html

[13] O. Cherepkova and J. Y. Hardeberg, "Enhancing dermoscopy images to improve melanoma detection," *2018 Colour and Visual Computing Symposium (CVCS), Gjovik, Norway*, 2018, pp. 1-6.

[14] "AUTO ENHANCEMENT FOR IMAGES," AUTO ENHANCEMENT FOR IMAGES - File Exchange - MATLAB CentralFile Exchange - MATLAB Central, May 28, 2009. Available: https://se.mathworks.com/matlabcentral/fileexchange/24290-auto-enhancement-for-images

[15] N. J.-Y. Huo, N. Y.-L. Chang, N. J. Wang, and N. X.-X. Wei, "Robust Automatic White Balance Algorithm using Gray Color Points in Images," *IEEE Transactions on Consumer Electronics*, Vol. 52, No. 2, 2006, pp. 541–546.

[16] A. Kumar, G. Hamarneh, and M. S. Drew, "Illumination-based transformations improve skin lesion segmentation in dermoscopic images," *2022 IEEE/CVF Conference on Computer Vision and Pattern Recognition Workshops (CVPRW)*, 2020, pp. 3132–3141.

[17] G. D. Finlayson, M. S. Drew, and C. Lu, "Intrinsic images by entropy minimization," in *Lecture notes in computer science*, 2004, pp. 582–595.

[18] U. Jamil, M. U. Akram, S. Khalid, S. Abbas, and K. Saleem, "Computer based melanocytic and Nevus image enhancement and segmentation," *BioMed Research International*, Vol. 2016, pp. 1–13, Jan. 2016.

[19] T. Sreelatha, M. V. Subramanyam, and M. N. G. Prasad, "Early Detection of Skin Cancer Using Melanoma Segmentation technique," *Journal of Medical Systems*, Vol. 43, No. 7, 2019.

[20] U. Jamil, A. Sajid, M. Hussain, O. Aldabbas, A. Alam, and M. U. Shafiq, "Melanoma segmentation using bio-medical image analysis for smarter mobile healthcare," *Journal of Ambient Intelligence and Humanized*

Computing, Vol. 10, No. 10, 2019, pp. 4099–4120.

[21] R. L. Araújo, F. H. D. De Araújo, and R. R. V. E. Silva, "Automatic segmentation of melanoma skin cancer using transfer learning and fine-tuning," *Multimedia Systems*, Vol. 28, No. 4, 2021, pp. 1239–1250.

[22] N. Otsu, "A Threshold Selection Method from Gray-Level Histograms," *IEEE Transactions on Systems Man and Cybernetics*, Vol. 9, No. 1, 1979, pp. 62–66.

[23] H. Lee and K. Kwon, "Diagnostic techniques for improved segmentation, feature extraction, and classification of malignant melanoma," *Biomedical Engineering Letters*, Vol. 10, No. 1, 2019, pp. 171–179.

[24] D. R. Ramani and S. S. Ranjani, "An efficient melanoma diagnosis approach using integrated HMF Multi-Atlas map based segmentation," *Journal of Medical Systems*, Vol. 43, No. 7, 2019.

[25] B. Zhang et al., "Short-Term lesion change detection for melanoma screening with novel Siamese neural network," *IEEE Transactions on Medical Imaging*, vol. 40, no. 3, 2020, pp. 840–851.

[26] Z. Yu et al., "Early melanoma diagnosis with sequential dermoscopic images," *IEEE Transactions on Medical Imaging*, Vol. 41, No. 3, 2021, pp. 633–646.

[27] K. Hu et al., "Classification of melanoma based on feature similarity measurement for codebook learning in the bag-of-features model," *Biomedical Signal Processing and Control*, Vol. 51, 2019, pp. 200–209.

[28] A. Mahbod, G. Schaefer, I. Ellinger, R. Ecker, A. Pitiot, and C. Wang, "Fusing fine-tuned deep features for skin lesion classification," *Computerized Medical Imaging and Graphics*, Vol. 71, 2018, pp. 19–29.

[29] P. M. M. Pereira et al., "Melanoma classification using light-Fields with morlet scattering transform and CNN: Surface depth as a valuable tool to increase detection rate," *Medical Image Analysis*, Vol. 75, 2021, p. 102254.

[30] R. Kaur, H. GholamHosseini, R. Sinha, and M. Lindén, "Automatic lesion segmentation using atrous convolutional deep neural networks in dermoscopic skin cancer images," *BMC Medical Imaging*, vol. 22, no. 1, 2022.

[31] M. N. Qureshi, M. S. Umar, and S. Shahab, "A Transfer-Learning-Based Novel Convolution neural network for melanoma classification," Computers, Vol. 11, No. 5, 2022, p. 64.

[32] R. Raza, F. Zulfiqar, S. Tariq, G. B. Anwar, A. B. Sargano, and Z. Habib, "Melanoma Classification from Dermoscopy Images Using Ensemble of Convolutional Neural Networks," *Mathematics*, Vol. 10, No. 1, 2021, p. 26.

[33] J. Ding, J. Song, J. Li, J. Tang, and F. Guo, "Two-Stage deep neural network via ensemble learning for melanoma classification," *Frontiers in Bioengineering and Biotechnology*, Vol. 9, 2022.

[34] P. Ghosh et al., "SkinNet-16: A deep learning approach to identify benign and malignant skin lesions," *Frontiers in Oncology*, Vol. 12, 2022.

[35] O. Ronneberger, P. Fischer, and T. Brox, "U-NET: Convolutional Networks for Biomedical Image Segmentation," *in Lecture notes in computer science*, 2015, pp. 234–241.

[36] S. Feng et al., "CPFNET: Context Pyramid Fusion Network for Medical Image Segmentation," *IEEE Transactions on Medical Imaging*, Vol. 39, No. 10, 2020, pp. 3008–3018.

[37] Z. Gu et al., "CE-NET: Context Encoder Network for 2D medical Image Segmentation," *IEEE Transactions on Medical Imaging*, vol. 38, no. 10, 2019, pp. 2281–2292.

[38] H. Wu, S. Chen, G. Chen, W. Wang, B. Lei, and Z. Wen, "FAT-Net: Feature adaptive transformers for automated skin lesion segmentation," *Medical Image Analysis*, Vol. 76, 2021, p. 102327.

[39] Z. Yu, L. Yu, W. Zheng, and S. Wang, "EIU-Net: Enhanced feature extraction and improved skip connections in U-Net for skin lesion segmentation," *Computers in Biology and Medicine*, Vol. 162, 2023, p. 107081.